Science Advances

AAAS

advances.sciencemag.org/cgi/content/full/2/2/e1501272/DC1

Supplementary Materials for

Ion transport in complex layered graphene-based membranes with tuneable interlayer spacing

Chi Cheng, Gengping Jiang, Christopher J. Garvey, Yuanyuan Wang, George P. Simon, Jefferson Z. Liu, Dan Li

Published 12 February 2016, *Sci. Adv.* **2**, e1501272 (2016)
DOI: 10.1126/sciadv.1501272

The PDF file includes:

Section I. Fabrication of the LGG membranes
Section II. Tuning the average interlayer spacing through the capillary compression method
Section III. Determination of the average interlayer spacing from membrane thickness
Section IV. Small-angle neutron scattering of the compressed LGG membranes
Section V. Time-lag diffusion and electrokinetic ion transport experiments
Section VI. Continuum modeling of concentration-driven ion diffusion through the cascading nanoslits contained in the LGG membranes
Section VII. Continuum modeling of electrokinetic ion transport through the cascading nanoslits contained in the LGG membranes
Fig. S1. A schematic showing the fabrication of the LGG membranes and tuning of the interlayer spacing.
Fig. S2. Isotropic SANS patterns of the compressed LGG membranes.
Fig. S3. Concentration-driven ion transport through the LGG membranes.
Fig. S4. Effect of circulation rate on ion permeation through the LGG membranes.
Fig. S5. The continuum simulation model for steady-state diffusion across charge-neutral cascading nanoslits.
Fig. S6. Determination of the geometrical variables L and δ through a reverse Monte Carlo method.
Fig. S7. The continuum simulation model for steady-state diffusion across negatively charged cascading nanoslits.
Fig. S8. Concentration and electric potential distribution profiles of the steady-state KCl diffusion across negatively charged cascading nanoslits.
Fig. S9. An AFM image of CCG on mica substrates.

Fig. S10. Continuum simulations of the electrokinetic ion flow across negatively charged cascading nanoslits.
Fig. S11. Representative *I-V* curves of the electrokinetic ion transport measurements.
Fig. S12. Typical *I-V* curves for the establishment of membrane selectivity.
Fig. S13. The increase in channel concentration as a result of channel surface charge.
Fig. S14. Scaling behaviors of the electrokinetic ion transport as a function of channel size across the range of sub–10 nm and of varied ionic concentrations.
Fig. S15. The continuum simulation model for electroosmotic current across the negatively charged cascading nanoslits.
Table S1. Geometries of the cascading nanoslits model.
Table S2. Effect of surface charge status on ion diffusion coefficient across the cascading nanoslits.
References (*56*–*72*)

Section I. Fabrication of the LGG membranes

Chemically converted graphene (CCG) dispersion was synthesized by following the method we previously reported (*56*). Briefly, graphene oxide aqueous colloid (0.5 mg/ml, 100 ml) was mixed with 0.2 mL hydrazine (35 wt% in water) and 0.35 mL ammonia solution (28 wt% in water) in a glass vial. After being vigorously shaken for a few minutes, the vial was put in a water bath (~100 ^{o}C) for 3 hours.

The original layered graphene gel (LGG) membranes were fabricated by following the method we previously reported (the membrane samples had not been subjected to capillary compression at this stage) (*33*). A controlled amount of as-obtained CCG dispersion was vacuum filtrated through a mixed cellulose ester filter membrane (0.05 μm pore size). The vacuum was disconnected immediately after no free CCG dispersion remained on the filtrate cake. The LGG membranes were then carefully peeled off from the filter membrane, immediately transferred to a Petri dish and immersed in water overnight to further remove the remaining ammonia and unreacted hydrazine (fig. S1, the 'vacuum filtration' step). To ensure sufficient mechanical robustness of the freestanding membranes, CCG mass loading of all LGG membrane samples was controlled to be 1.0 mg/cm^2.

Section II. Tuning the average interlayer spacing through the capillary compression method

Interlayer spacing among the CCG sheets inside the LGG membranes was collectively tuned via a capillary compression procedure, as we have previously reported (*34*). Briefly, the water inside the as-assembled gel membranes was first exchanged with a ratio-controlled volatile/nonvolatile miscible solution. The volatile liquid inside the gel membranes was then selectively removed through vacuum evaporation. The removal of volatile part of the miscible solution exerted capillary compression between CCG layers, leading to uniform shrinkage of membrane thickness and thereby statically decreasing the average interlayer spacing. As the nonvolatile part of the miscible solution in the gel membrane remained, the average interlayer spacing was readily tuned by adjusting the ratio of volatile/nonvolatile solutions. Subsequently, the as-compressed

gel membranes were washed thoroughly with deionized water, exchanging the nonvolatile liquid back to water prior to ion transport tests (the last step shown in fig. S1). It was found that the gel membranes would swell to a certain degree during the final washing step. Accordingly, sample thickness was determined after thorough wash with deionized water and immersed in correspond testing solutions, prior to all ion transport experiments. In this work, the volatile/nonvolatile miscible solution was sulfuric acid aqueous solutions of various acid concentrations, namely 5.0 M, 3.0 M, 2.0 M, 1.0 M, 0.5 M, 0.3 M, 0.2 M and 0.05 M.

Section III. Determination of the average interlayer spacing from membrane thickness

The CCG sheets were found oriented in a face-to-face, multilayered configuration in the LGG membranes. By fixing the areal mass loading to be 1 mg/cm^2, estimation of the average interlayer spacing directly from the thickness of the membranes was made according to the formula

$$d_{\exp} = \frac{\text{Areal density of graphene} \times \text{thickness of the gel membranes}}{\text{Areal mass loading of the gel membranes}} \quad (1)$$

where the areal mass density of graphene is reported to be 0.77 mg/m^2 (*57*). The thickness of the LGG membranes was measured using a digital micrometre at 1 μm resolution. Having considered the measuring resolution of the digital micrometre, a 10% error was given to measurements of gel membrane samples with thicknesses larger than 10 μm, and a 15% error to samples with thickness smaller than 10 μm. According to equation (1), the other source of error associated with the calculation of d_{exp} was from the use of areal mass density of pristine graphene. As extensively discussed in this work, the layered structure in real samples is imperfect on many levels and across multiple length scales including the in-plane defects/holes, corrugated configuration on molecular level, irregular sheet size and shape as well as the gaps between the edge of the sheets on micrometre scales. Therefore, the true statistical expectation of the interlayer spacing was smaller than as-calculated d_{exp}. Nonetheless, the smallest value of d_{exp} calculated from membrane thickness in our work was 0.5 nm, approaching the lower limit of graphene-based layered materials, which is 0.335 nm as found in graphite crystals (*58*).

Therefore, the length scales of interlayer spacing in the LGG membranes in this work lay justifiably within the range of sub-10 nm.

Section IV. Small-angle neutron scattering of the compressed LGG membranes

The small-angle neutron scattering (SANS) experiments were carried out using QUOKKA the reactor-based pin-hole instrument at the Australian Nuclear Science and Technology Organization (ANSTO, Lucas Heights, Australia). The measurement was performed in transmission mode, with the average membrane plane aligned perpendicular to the illuminating neutron beam. In these SANS experiments, a 10 mm collimated beam of neutrons was used to illuminate the sample. The samples were sandwiched between two quartz slides and held in a movable multi-sample changer with SANS measured in transmission mode at sample to detector distances of 1.4, 6.0 and 14.0 m for 5 Å neutrons and 20 m in a focusing optics configuration using 8 Å neutrons. SANS 2D patterns were isotropic and the reduction to the 1D SANS data involved radial averaging after correction for background scattering; sample and cell transmission; and the detector efficiency. The data was converted to absolute scattering cross-section by scaling to the incident flux of neutrons and normalized to the sample thickness. These operations were performed using IgorPro (Wavemetrics, Lake Oswego) macro's (*59*) especially written for reduction of the raw 2D data to the 1D absolute intensity versus q, defined as

$$q = 4\pi \sin(\frac{\theta}{\lambda}) \tag{2}$$

where 2θ is the scattering angle defined by the measurement geometry. The reduced 1D SANS data were then offset to show the shape of each curve and for better comparison. Finally, linear regression was applied to the data set in the q range from 0.001 to 0.01 $Å^{-1}$ on log-log scale; the slope F was then obtained and compared. As the SANS experiments could take up to ~5 hours for each sample at a long sample-to-detector distance of 20 m, to ensure reliable measurements we used gel membranes at a state before final wash with deionized water (see the illustration in fig. S1). The nonvolatile liquid trapped inside the gel membranes would minimize potential structural variation caused by evaporation. In this case, the average intersheet spacing was calculated according to the sample thickness at the same state when the SANS was performed, which was measured without the final wash or the "exchange of liquid" step.

Section V. Time-lag diffusion and electrokinetic ion transport experiments.

Concentration-driven ion diffusion through the LGG membranes

The concentration-driven diffusion experiments were performed on a device composed of two reservoirs, separated by the LGG membranes under investigation (Fig. 2A). The membranes were first thoroughly washed with deionized water and sealed with two O-rings before being clamped onto a home-made membrane holder with an opening of 4.9 mm in diameter. In a typical experiment, one compartment (referred to as the feed) was filled with 40 mL 0.5 M KCl, while the other (permeate) compartment was filled with the same amount (40 mL) deionized water. The two compartments were symmetrically equivalent in size and shape, and were carefully covered so as to ensure that the solution levels in both compartments remained the same throughout the entire diffusion process. The amount of ion permeating through the LGG membranes was continuously monitored by an electrical conductivity probe. The duration for each permeation test was sufficiently long to allow the permeation curve to be dominated by the steady-state diffusion, which was reflected by a linear relationship between permeate amount and elapsed time (fig. S3A). The reproducibility of the permeation experiments was repeatedly checked by measuring the permeation rate of one sample for three times (fig. S3B). The membrane permeation rate was determined by calculating the slope of the steady-state diffusion curve. To ensure that the concentration difference between the feed and permeate compartments remained constant, and that ion permeation was driven solely by this concentration gradient, no readings were made after the concentration in the permeate compartment reached 1.4×10^{-3} M (over two orders of magnitude smaller than the original concentration difference set as 0.5 M). Solutions in both the feed and permeate compartments were constantly circulated, to avoid possible concentration gradient build-ups at the membrane surfaces.

Membrane continuity assessment

As the interlayer spacing between corrugated CCG multilayers were tuned collectively in a range from sub-nanometre to ~10 nm, it essentially forms pores that run though the LGG membranes. This makes the LGG membranes a class of porous membrane. It is crucial to ensure that their

pore structure remains intact during the permeation experiment, and that the measured permeation rate is reproducible. The circulation flow rate in both the feed and permeate compartments was varied so that its effect on permeation rate could be determined, and used to assess the membrane's structural integrity and the reproducibility of the permeation experiments. In a typical check, the membrane permeability was measured under different levels of circulation flow rates generated using a peristaltic pump, namely at rates of 10.7, 12.9 and 30 mL/min. The circulation rate was continually raised while the membrane permeability was measured and determined from the slope of diffusion curve in the steady-state region. As ions diffused through the membrane, concentration close to the membrane surface on the feed side decreased, whilst it increased on the permeate side. This lowered the trans-membrane concentration gradient during the transient-state of diffusion (refer to the *time-lag determination of membrane diffusivity in Ref.*(*41*)), and thus significantly extended the duration needed for a steady-state diffusion to be established. When the steady-state was reached, such a decrease in trans-membrane concentration gradient was minimized. If the membranes remained structural intact, without pinholes disrupting the alignment of CCG sheets, the variance in circulation would not affect permeation rate as shown in fig. S4.

Electrokinetic ion transport through the LGG membranes

Electrokinetic ion transport measurements were carried out in a U-shaped device separated by the LGG membranes. The membranes were mounted onto the same membrane holder as used for ion permeation experiments. All devices were thoroughly rinsed with deionized water prior to use. The ion transport resistance across the membranes was derived from *I-V* curves (fig. S11). For each measurement, four current densities, (namely ±100 and 200 nA, ±500 and 1000 nA and ±5 and 10 μA, for electrolyte concentrations of 1 mM, 10 mM, 100 mM, respectively) were symmetrically chosen below and above 0 V and corresponding voltage drops were recorded to calculate the resistance of the device. The *I-V* curves of all samples showed good linear characteristics which extended to the origin. To obtain membrane resistance, the resistance of the device without the membrane was subtracted from the resistance of the device with the membrane (*42*). All electrodes used for applying electrical current and recording voltage drop

were made of Ag/AgCl. The measurement of each sample was repeated three times in a temperature-controlled environment (22 °C ~ 23 °C).

The dependence of ionic concentration was investigated by varying the concentration of KCl electrolytes from 1 mM, 10 mM to 100 mM. The measurement was always commenced from low concentrations, moving up to higher concentrations.

Membrane selectivity measurement

An established and immediate measurement of ion selectivity is to set up a concentration gradient over the membrane, in our case 10 and 100 mM KCl aqueous solutions on each side of the LGG membranes (*50*). This creates a driving force for diffusion of both K^+ and Cl^-. If one type of ions can pass through the membrane quicker than the other, then there will be a measureable net current flow across the membrane when the trans-membrane potential is set as zero. This current can be stop by applying an opposing electric field. The corresponding voltage (the reversal potential) can be used to assess the selectivity of membranes. As derived from Nernst equation, an ideal/fully selective membrane will have a reversal potential of 58 mV per ten-fold change in concentration gradient. We sealed the LGG membrane using the same clamp device used for both diffusion and electrokinetic ion transport measurements. Ag/AgCl electrodes were used to record the *I-V* curves (fig. S12). To ensure the electrode potential remain constant, we inserted the Ag/AgCl electrode on the 10 mM KCl side in a capillary filled with 100 mM KCl solution. *I-V* curves were recorded in a voltage range from -0.2 to 0.2 V.

Section VI. Continuum modeling of concentration-driven ion diffusion through the cascading nanoslits contained in the LGG membrane

We used the COMSOL Multiphyscis simulation package to perform continuum modeling of the ion transport through the cascading nanoslits contained in the LGG membranes. The governing equations were Poisson-Nerst-Plank equation and Navier-Stokes equation. It is well accepted in the nanofluidic community that for channel size above ~1 nm, these classic continuum theories generally apply (*9, 10, 13, 60*).

Figure S5 shows our continuum model of the cascading nanoslits in the LGG membranes. The CCG layers (represented as white thin rectangles) were stacked face-to-face in a layered fashion. As proposed in this work, we assumed an ordered microstructure (same as shown in Fig. 1B), in which all layers had the same lateral length and were separated by the same intersheet distance. The model had three variables namely, the size of individual nanosheets L (note that sheets in the model were assumed flat and impermeable to ions), gap distance between the sheets δ and intersheet distance d. We assigned 20 layers to the cascading nanoslits model, which allowed convergence of simulation results without much computational expense. Each layer was 0.335 nm in thickness adopted from the d in graphite crystals (*58*). The mesh structure was generated sufficiently dense to ensure the convergence of the results.

Simulation of steady-state ion diffusion

When the steady-state diffusion was reached, the ions migrated in cation/anion pairs as a result of columbic interactions, and there was no net water flux from feed to permeate or vice versa. As K^+ and Cl^- have similar diffusion coefficient in water (*61*), we thus treated the diffusion of KCl as that of neutral particles with a mean diffusivity of 1.8×10^{-5} cm^2/s (*62*), whilst the background water was immobilized. We adopted the Fick's law

$$\frac{\partial C_i}{\partial t} = D_i \nabla^2 C \tag{3}$$

where D_i and C_i are the diffusivity and concentration of ion type i, to describe the diffusion of neutral particles. Boundary conditions were set as follows:

1) at the CCG/electrolyte interface,

$$\nabla_{\perp} C_i = 0 \tag{4}$$

2) the top and bottom periodic boundary condition (PBC),

$$\nabla_{\perp} C_i = 0 \tag{5}$$

3) the concentration at the entrance (left end colored in blue),

$$C_i = 0.5 \text{ M} \tag{6}$$

4) the concentration at the exits (right end colored in red),

$$C_i = 0 \text{ M} \tag{7}$$

The initial concentration inside the cascading nanoslits was set at 0 M, and the concentration difference was ΔC = 0.5 M.

The time-dependent diffusion modeling was undertaken to record the mean diffusion flux of the neutral particles at the right exits that went across the cascading nanoslits J(t). The time-span of modeling was varied from 1~5000 ns according to the structure of the cascading nanoslits. The duration of the modeling was allowed to be sufficiently long (6000~70000000ns) so as to ensure a steady-state was reached ($\Delta J(t)/J(t) < 10^{-6}$).

The ion diffusivity across the cascading-nanoslit-structured membrane, denoted as $D_{m,sim}$, was calculated as,

$$D_{m,\,sim} = \frac{J(\infty)t_m}{\Delta C} \tag{8}$$

where $J(\infty)$ is the flux of neutral particles at the steady state, t_m the membrane thickness and ΔC the cross-membrane concentration difference.

We performed a series of modeling experiments where the values of L, δ and d were varied to create a 3D data space (19×6×6) for $D_{m,sim}$. To ensure the data space covered all possible geometrical configurations of the cascading nanoslits, the ranges of L, δ and d were set as 8~1000 nm, 0.5~12 nm and 1~20 nm respectively. Figure 3 shows the profile of the as-calculated $D_{m,sim}$ against varied L, δ and d.

Determination of the geometrical configuration of the cascading nanoslit model

A reverse Monte Carlo method was applied to locate the best geometrical parameters, L and δ, of the cascading nanoslit model through minimization of the difference (min{Δ}) between the modeling data and experiment results.

$$\min\{\Delta\} = \min \sum_{i=1} [\tilde{D}_{m,\,sim}(L, \delta, d_i) - D_{m,\,\exp}(d_i)]^2 \tag{9}$$

where d_i is the intersheet distance of the ith LGG membrane measured in the experiment, $D_{m,exp}(d_i)$ is the experimentally measured diffusivity of the LGG membrane with the interlayer spacing of d_i. $D_{m,sim}(L, \delta, d_i)$ is the linear interpolation of $D_{m,sim}$ calculated with a set of L, δ and d from the 3D data space. Since $D_{m,exp}(d_i)$ has a larger value when d is large, effectively the results from the LGG membranes with larger d play a more dominant role in the fitting. It should also be noted that in this modeling it was assumed that the value of L and δ remained constant as d was tuned. This assumption is based on the experiment observations that the macroscopic dimension of the LGG membranes changed largely along the thickness direction while the membranes were subjected to the capillary compression procedure (*33, 34*).

Previous research has shown that ion diffusivity is expected to decrease when confined in nano-sized space (*45*). Therefore, the effect of a possible hindrance factor $H(\lambda)$ (shortened as H in the main text) adopted from the Dechadilok and Deen's model for the cascading nanoslit model on the ion diffusivity $D_{m,sim}$ was also considered

$$H(\lambda) = 1 + \frac{9}{16}\lambda \ln \lambda - 1.19358\lambda + 0.4285\lambda^3 - 0.3192\lambda^4 + 0.08428\lambda^5 \tag{10}$$

where λ is the relative solute size, that is the ratio of solute diameter divided by the height of slit channel. Solvated ions K^+ and Cl^- were comparable in size. The Stokes radius of K^+ is $r_{K^+} = 0.12$ nm (*63*) and these values were then used to determine $\lambda = 2r_{K+}/d$. In these terms, the minimization in the reverse Monte Carlo method was modified as follows:

$$\min\{\Delta\} = \min \sum_{i=1} [H(\lambda)\tilde{D}_{m,sim}(L,\delta,d_i) - D_{m,\exp}(d_i)]^2 \quad (11)$$

A million pairs of varied L and δ were compared in each loop. The range of parameters in the first loop was 8 nm $\leq L \leq$ 1000 nm and $1 \leq \delta \leq 20$ nm with known $d = d_{exp}$ as measured in the experiments. The range of parameters was gradually reduced for each loop. The values of L and δ at the top 20% fitting in the previous loop were taken as the parameter ranges for the next loop. The ranges of L and δ were found rapidly convergent after 10 loops (fig. S6), and the values of L and δ were able to be determined after 100 loops. Table 1 summarizes the results.

Effect of CCG surface charge on ion diffusion through the cascading nanoslit model

We also investigated the impact of the surface charges on CCG sheets on steady-state ion diffusion across the cascading nanoslits. Two reservoirs of 100 nm in length were added to both sides of the cascading nanoslits model to control the electric potential and concentration at the boundaries. Because the accurate surface charge status of the CCG sheets in the LGG membranes was unknown, we chose a range based on the previous experimental work (*46*) from σ = -2.3 mC/m^2 for CCG materials to an exaggeratingly high σ = -56.1 mC/m^2, which is comparable to that of graphene oxide, so as to cover all possible surface charge possibilities of the CCG in our experimental systems. We doubled the overall layers to 40 to reduce the edge effects arisen from surface-charge-induced electric field both at the entrances and exits (fig. S7). Continuum modeling was performed and the concentration field of both K^+ and Cl^- (C_{K^+} and C_{Cl^-}) and the electric potential field (Φ) were rendered in fig. S8.

The discussions of the effect of surface charge on ion diffusion through the nanoslits were made only on the systems where the interlayer spacing is sufficiently large (d = 4.5 ~ 11 nm) so that the validation of continuum theories acceptably hold. As a demonstration, we chose the geometrical variables L = 50 nm, δ = 1.6nm. The governing equation for concentration gradient and electric potential is Poisson-Nernst-Plank (PNP) equation,

$$\frac{\partial C_i}{\partial t} = D_i \nabla^2 C_i + z_i e \mu_i C_i \nabla \Phi - \vec{u} \nabla Ci \tag{12}$$

where z_i is the valence number of particle type i, e is the elementary charge, μ_i is the mobility of ions ($\mu_{K+} = 7.6\times10^{-8}$ and $\mu_{Cl-} = 7.91\times10^{-8}$ $m^2\,V^{-1}\,s^{-1}$)(*15*), Φ is the local electric potential, **u** is the local background flow vector (for the stationary state, **u** is zero). D_i is the diffusivity of particle type i, which is calculated according to Einstein–Smoluchowski relation:

$$D_i = u_i k_B T \tag{13}$$

where T is the temperature set as 300K in this modeling, k_B is the Boltzmann constant. The charge-density-induced electric potential field is described by the Poisson equation,

$$\nabla^2 \Phi = \frac{F}{\varepsilon_w \varepsilon_0} \sum_i z_i C_i \tag{14}$$

where ε_w is 80, the relative permittivity of water (*64*, *65*) and ε_0 is the vacuum permittivity, F is the Faraday constant.

The boundary conditions applied to the system were set as follows,

1) at the CCG/electrolyte interface,

$$\nabla_\perp C_i = 0 \tag{15}$$

$$(\varepsilon_w - \varepsilon_G)\nabla_\perp \Phi = -\frac{\sigma}{\varepsilon_0} \tag{16}$$

Where σ is the surface charge on the CCG sheet and ε_G is the dielectric constant of graphene sheet (4 in this simulation). Note that different boundary conditions were set for the electric potential and concentration field. The finite dielectric constant of graphene provided a permeable electric potential field. The dielectric constant of pristine graphene has a value from 2~15, which is still an subject of debate (*66-69*). Fortunately, the variance of ε_G was found to have a quite small effect on the simulation result.

2) the upper and bottom periodic boundary conditions,

$$\nabla_{\perp} C_i = 0 \qquad \nabla_{\perp} \Phi = 0 \tag{17}$$

3) concentration and electric potential at the entrance (left end colored in blue),

$$C_i = 0.5 \text{ M} \qquad \Phi = 0 \tag{18}$$

4) concentration and electric potential at the exit (right end colored in red),

$$C_i = 0 \text{ M} \qquad \nabla_{\perp} \Phi = 0 \tag{19}$$

No electric potential control was applied to the system and the left end was grounded to zero.

We performed time-independent simulations for steady-state diffusion across the charged cascading nanoslits. Stationary solutions of ion flux J_{K+} and J_{Cl-} were given, which were the same as in the time-dependent simulation.

The concentration drop was linear in reservoirs on each side (fig. S8). The concentration drop across cascading-nanoslit-structured membrane was calculated according to,

$$\Delta C_m = \Delta C - 2\Delta C_{res} = \Delta C - 2\frac{J_{KCl}}{D_{KCl,\,bulk}} L_{res} \tag{20}$$

where ΔC_{res} is the concentration drop in each reservoir, L_{res} is the length of the reservoir, J_{KCL} is the mean diffusion flux of KCl ($J_{KCL} = (J_{K^+} + J_{Cl^-})/2$) and $D_{KCl,bulk}$ is the mean diffusivity of KCl in bulk solution ($D_{KCl,bulk} = (D_{K^+} + D_{Cl^-})/2$). We calculated the mean diffusivity $D_{m,sim}$ of KCl across the cascading nanoslits, which was then compared to that in bulk (Table S2). As the real surface charge status of CCG layers in the LGG membranes was unknown, a range of surface charge based on the previous experimental work was chosen (*46*). When the surface charge status of CCG was assumed to be comparable to that measured by experiment (σ = -2.3 mC/m^2), corresponding influences on $D_{m,sim}$ were quite small ~ 2%. Even when the surface charge was assumed to be extremely high (approaching the value of graphene oxide, σ = -56 mC/m^2), the variance in $D_{m,sim}$ was only ~ 15%. It was clear that the effect of surface charge on diffusivity of

the membranes was quite small. Therefore, the surface charge effect was neglected in the reverse Monte Carlo determination of the geometrical parameters of the cascading nanoslits model.

Diffusioosmosis effects

It is also known that ion diffusion through smooth nanochannels might cause appreciable osmotic flow, especially for graphene/carbon-based channels that have been reported to have a possibly large slip length (*43, 44*). Nevertheless, for steady-state diffusion, the net water flux across the nanoslits remains zero. Considerations of such an osmotic water flow were thus avoided in our simulations.

Effect of L on D_m

In our simulations, the individual sheet size L determined through the reverse Monte Carlo method was in a range of ~50 nm, which was much smaller than that typically reported in the literature ~ 1 μm obtained from SEM/AFM imaging (*28*). This result is consistent with reports that there are a considerable amount of intrinsic pores on the CCG plane having a size sufficiently large to allow ions to pass through (*70*). This finding in return suggests that an overestimation of D_m across the nano-capillaries embedded in multilayered graphene-derived-nanosheet membranes could occur if D_m is directly calculated using the cascading nanoslit model with lateral size values determined through SEM/AFM imaging, in which case the presence of in-plane pores is not considered. In addition, the lateral size is effectively a broad distribution from tens of nanometres up to several micrometres for both CCG and graphene oxide materials systems, which is the result if followed the synthesis route of chemical exfoliation and reduction (*71*). In light of the presence of in-plane pores and a large distribution of sheet sizes, extra caution is needed in the case where D_m is estimated solely based on a structural model with the size of the nanosheets determined by microscopy.

Section VII. Continuum modeling of electrokinetic ion transport through the cascading nanoslits embedded in the LGG membranes

Figure S10 shows our simulation model of the cascading nanoslits for electrokinetic ion transport. The governing equation was Poisson-Nernst-Planck (PNP) equation. Boundary conditions were set as follows,

1) at the CCG/electrolyte interface,

$$\nabla_{\perp} C_i = 0 \tag{21}$$

$$(\varepsilon_w - \varepsilon_G)\nabla_{\perp} \Phi = -\frac{\sigma}{\varepsilon_0} \tag{22}$$

2) the upper and bottom periodic boundary conditions,

$$\nabla_{\perp} C_i = 0 \qquad \nabla_{\perp} \Phi = 0 \tag{23}$$

3) concentration and electric potential at the left end (colored in blue),

$$C_i = C_0 \qquad \Phi = 0 \text{ V} \tag{24}$$

4) concentration and electric potential at the right end (colored in red),

$$C_i = C_0 \quad \Phi = 0.01 \text{ V} \tag{25}$$

where C_0 is concentration in the reservoirs which were varied from 1 mM, 10 mM to 100 mM and the electric potential difference $\Delta\Phi$ externally applied was 0.01 V.

Time-independent electrokinetic simulations were carried out with varied intersheet spacings, reservoir concentrations, and surface charge densities namely σ = -2.3, -11.2 and 56.1 mC/m^2. When the system reached a stationary state, the concentration of cation/anions in the nanochannels was analyzed (fig. S13), and the ion conductance in nanochannels was calculated and compared to that in bulk (fig. S14).

The resistance of the whole system including two reservoirs and the cascading-nanoslit-structured membrane was calculated as,

$$R = \frac{\Delta\Phi}{F(J_{K^+} - J_{Cl^-})A_m} = \frac{t_m}{\kappa_m A_m} + \frac{2 \times L_{res}}{\kappa_0 A_m} \tag{26}$$

where κ_0 is the conductivity of the reservoir (bulk solution) given by $\kappa_0 = F(\mu_{K^+}C_0 + \mu_{Cl^-}C_0)$, J_{K+} and J_{Cl-} are the electro-kinetic fluxes of K^+ and Cl^- through the system respectively. κ_m is the conductivity of cascading-nanoslit-structured membrane, and is derived from the above equation as:

$$\kappa_m = \frac{t_m}{[\frac{\Delta\Phi}{F(J_{K^+} - J_{Cl^-})} - \frac{2 \times L_{res}}{\kappa_0}]} \tag{27}$$

where t_m and A_m are the thickness and membrane area of the cascading-nanoslit-structured membranes.

Effect of electro-osmotic current

Electro-osmotic flow (EOF) is expected in nanochannels with polarized ion concentrations, and it is found to accelerate ion transport and thus increase the conductivity of nanochannels. As the magnitude of EOF is proportional to the strength of the externally applied electric field, which was very low in experiments (7.7×10^{-8} ~ 3.5×10^{-5} V/nm), it is accepted in the nanofluidic community that the effect of electro-osmosis can be neglected in classic continuum modeling.

Nevertheless, the reported large slip length of graphene surfaces may significantly accelerate water flow. We therefore considered its effect on EOF through the cascading-nanoslit-structured membranes. The geometrical parameters for the simulation were L = 50 nm, δ = 1.6 nm, d = 10.98 nm (the largest d chosen here is to exaggerate the influence of EOF in order to testify the robustness of the model) and the surface charge imposed was σ = -2.3 mC/m^2. One reason for

choosing a surface charge of -2.3 mC/m^2 is based on the experimental results of the CCG as reported in Ref.(*46*). The other reason is that in this modeling of the EOF in CCG-enclosed nanochannels, we assigned an exaggeratingly large slip length of 100 nm for CCG surface. As such, the surface charge of CCG, which is originated from the dissociation of some oxygen-containing groups on the CCG surface ought to be minimized. Three continuum fields were considered, the concentration field (C_{K^+} and C_{Cl^-}), the electric potential Φ, and the laminar water flow (**u**).

The governing equation for concentration and electric potential was PNP, and the evolution of laminar flow was described by the Navier-Stoke equation for impressible liquids ($\rho\nabla\cdot\mathbf{u} = 0$**)**.

$$\rho(\vec{u}\cdot\nabla)\vec{u} = \nabla\cdot[-P\vec{I} + \mu(\nabla\vec{u} + (\nabla\vec{u})^T)] + \vec{F} \tag{28}$$

where ρ and μ are the density and viscosity of water (1000 kg/m^3 and 8.94×10^{-4} Pa·s at 25 °C) (*72*), P is the local pressure, $\boldsymbol{I}$ is the identity matrix, **u** is the local flow vector and $\boldsymbol{F}$ is the external volumetric force. Thus for elecro-osmosis, the external volumetric force can be written as,

$$\vec{F} = F(C_{K^+} - C_{Cl^-})\nabla\Phi \tag{29}$$

where F is the Faraday constant and $\nabla\Phi$ is the local electric field. Clearly, as the induced water flow is caused by the outnumbered cations or anions in neutral channels, the contributions from cation and anion will cancel each other out which diminishes such EOF.

Boundary conditions were set as follows (fig. S15),

1) at the CCG/electrolyte interface,

$$\nabla_\perp C_i = 0 \tag{30}$$

$$(\varepsilon_w - \varepsilon_G)\nabla_\perp\Phi = -\frac{\sigma}{\varepsilon_0} \tag{31}$$

$$\mu_{\parallel} = \frac{L_s}{\mu}\tau_{\parallel} \tag{32}$$

where $u_{//}$ is the tangent velocity on the wall and $\tau_{//}$ is the tangent shear force on the interface, L_s is the slip length of the graphene wall. We imposed an exaggerated L_s = 100 nm for the graphene surfaces (*43*) to investigate how big an influence this would have on the induced EOF.

2) the top and bottom periodic boundary conditions,

$$\nabla_{\perp} C_i = 0 \tag{33}$$

$$\nabla_{\perp} \Phi = 0 \tag{34}$$

$$\tau_{\parallel} = 0 \tag{35}$$

$$u_{\perp} = 0 \tag{36}$$

where the "virtual" wall of top and bottom periodic boundary conditions can be eliminated by the complete slip boundary for water flow.

3) conditions at the left end (colored in blue),

$$C_i = C_0 \tag{37}$$

$$\Phi = 0 \text{ V} \tag{38}$$

$$P_{ext} = 0 \text{ for inlet} \tag{39}$$

4) conditions at the right end (colored in red),

$$C_i = C_0 \tag{40}$$

$$\Phi = 0.01 \text{ V} \tag{41}$$

$$P_{ext} = 0 \text{ for outlet} \tag{42}$$

where there is a potential difference for ion transport but no external pressure difference. The EOF induced has the same direction as the movement of the counter-ions (K^+ in this system) from right to left.

A potential drop of 0.01V imposed across the whole system resulted in an electric field cross the membrane of strength 2.34×10^{-5} V/nm, comparable to the maximum strength of electric field applied in our experiments. Stationary solutions for the electro-osmosis modeling showed a very weak EOF with a mean velocity of -4.08×10^{-7}m/s, significantly lower than the mean velocity of K^+ at both ends (-7.94×10^{-5} m/s and 8.07×10^{-5} m/s). Furthermore, the normalized channel conductance ($K_{m,sim\ (\sigma=-2.3)}/K_{m,sim\ (\sigma=0)}$) also showed a negligible difference between modeling results with ($K_{m,sim\ (\sigma=-2.3)}/K_{m,sim\ (\sigma=0)}$ = 0.07386) and without ($K_{m,sim\ (\sigma=-2.3)}/K_{m,sim\ (\sigma=0)}$ = 0.07378) EOF induced by the much exaggerated slip length of graphene surfaces (L_s = 100 nm) (*43*).

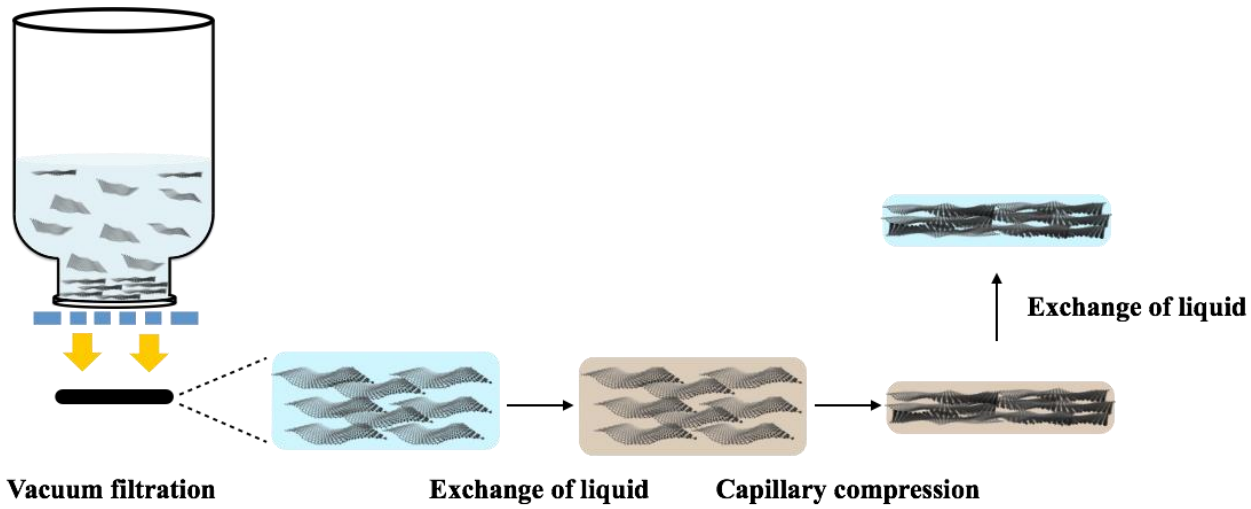

Fig. S1. A schematic showing the fabrication of the LGG membranes and tuning of the interlayer spacing. Four steps were included namely, vacuum filtration alignment of CCG sheets in water; exchange of the water trapped in between sheets to a volatile/nonvolatile miscible solutions (miscible water/H_2SO_4 mixture); capillary compression; and the exchange of the intersheet-trapped solutions back to water via thorough washing.

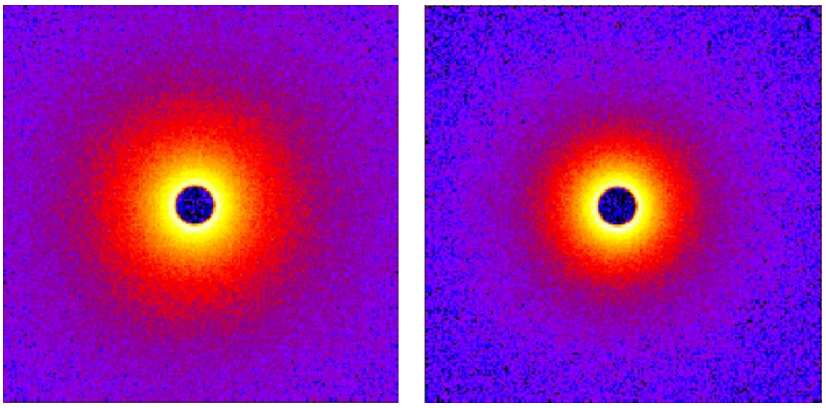

Fig. S2. Isotropic SANS patterns of the compressed LGG membranes. Through the capillary compression method previously reported (*34*), the membranes were compressed to various degrees with (left) d_{exp} = 7.0 nm and (right) 2.2 nm. The patterns showed a much stronger coherent scattering for samples with larger d_{exp}. The measurements were carried out with gel membranes without a final washing step and the nonvolatile H_2SO_4 liquid remained between the CCG layers.

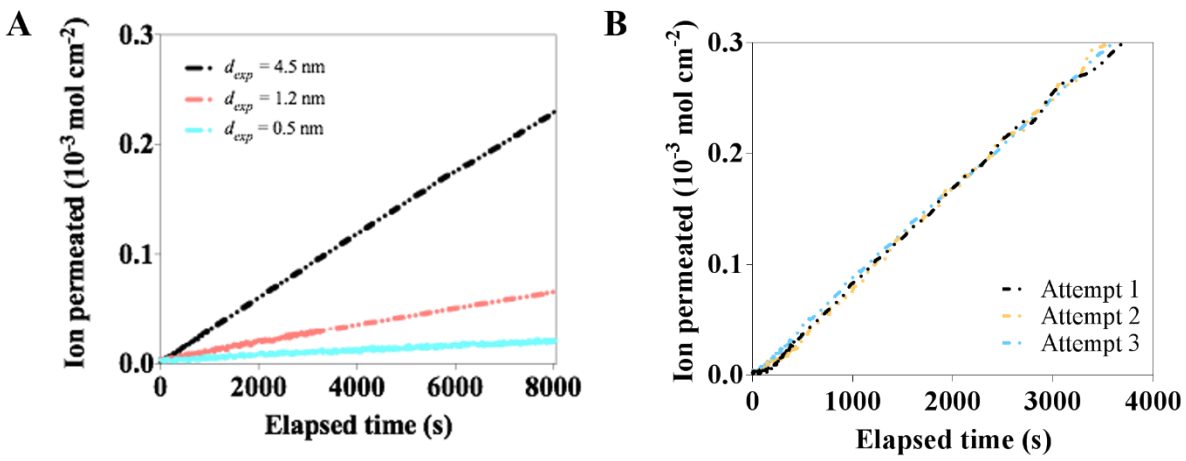

Fig. S3. Concentration-driven ion transport through the LGG membranes. (**A**) Ion permeation curves of the LGG membrane with d_{exp} = 0.5 nm, 1.2 nm and 4.5 nm. (**B**) Three overlapping permeation curves made on the same LGG membrane (d_{exp} = 16 nm) show good reproducibility of the diffusion experiment.

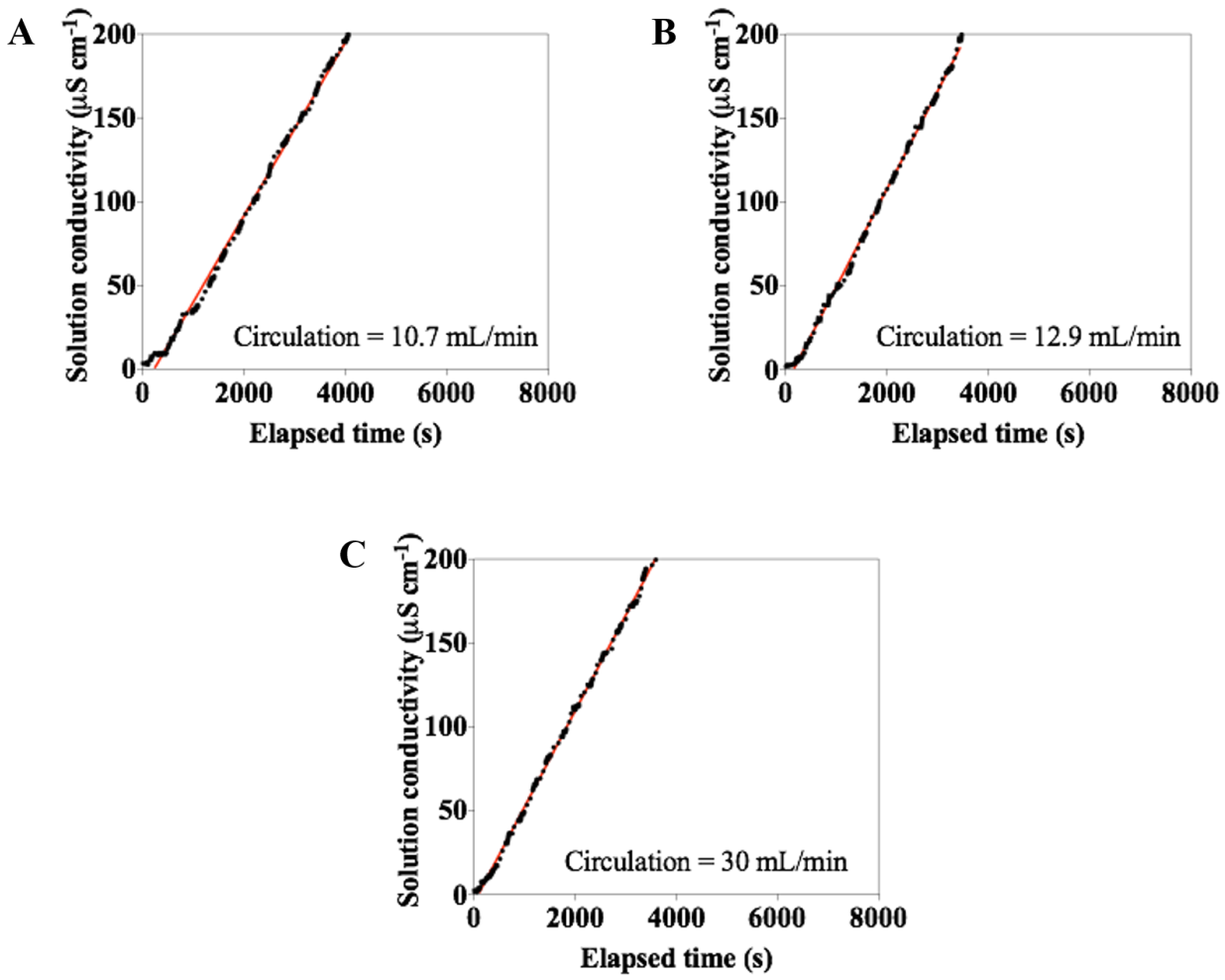

Fig. S4. Effect of circulation rate on ion permeation through the LGG membranes. Various levels of convection flow was generated via a peristaltic pump from (**A**)10.7 mL/min, (**B**)12.9 mL/min, to (**C**) 30 mL/min, resulting in a transition from transient state diffusion to steady-state state diffusion finishing at 543 s, 190 s to 68 s, respectively. This suggested that increasing the circulation rate accelerated the establishment of a stable concentration gradient across the membrane. However, a linear regression (red line) of the steady-state regions of the diffusion curves in the sequence of an increase in circulation rate gave largely unchanged slopes of 0.054, 0.059, and 0.057, respectively, which were directly proportional to permeation rate. The largely unchanged gradient values as a function of increase in circulation rates suggested the absence of pinholes through the membranes. The presence of pinholes would greatly decrease the tortuous pathways through the cascading nanoslits and significantly increase the measured permeation

rates, particularly when circulation rates were increased. The membranes tested had d_{exp} = 11 nm.

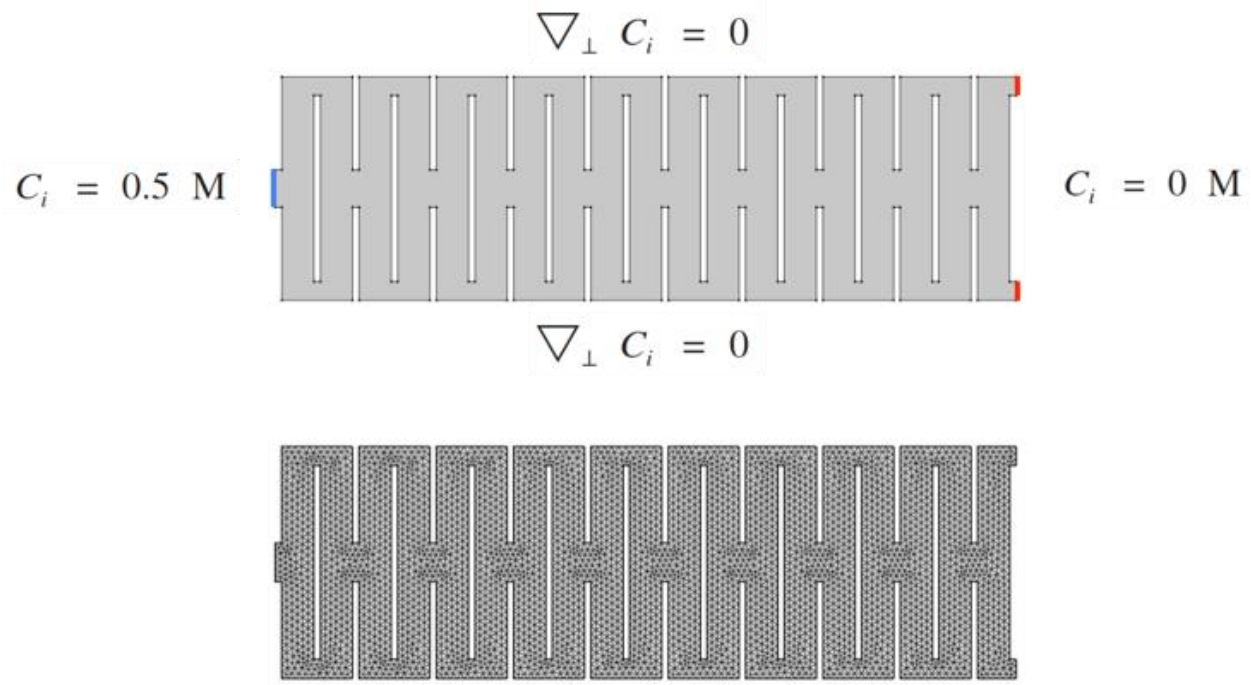

Fig. S5. The continuum simulation model for steady-state diffusion across charge-neutral cascading nanoslits. The simulation model, as shown in the figure at the top, consists of 20 layers of impermeable CCG sheets aligned into cascading nanoslits. The shaded region represents the cascading flow network through the nanoslits. Concentrations are fixed at both the left entrance (colored in blue) and the right exits (colored in red). The mesh structure generated via COMSOL software is shown in the figure at the bottom.

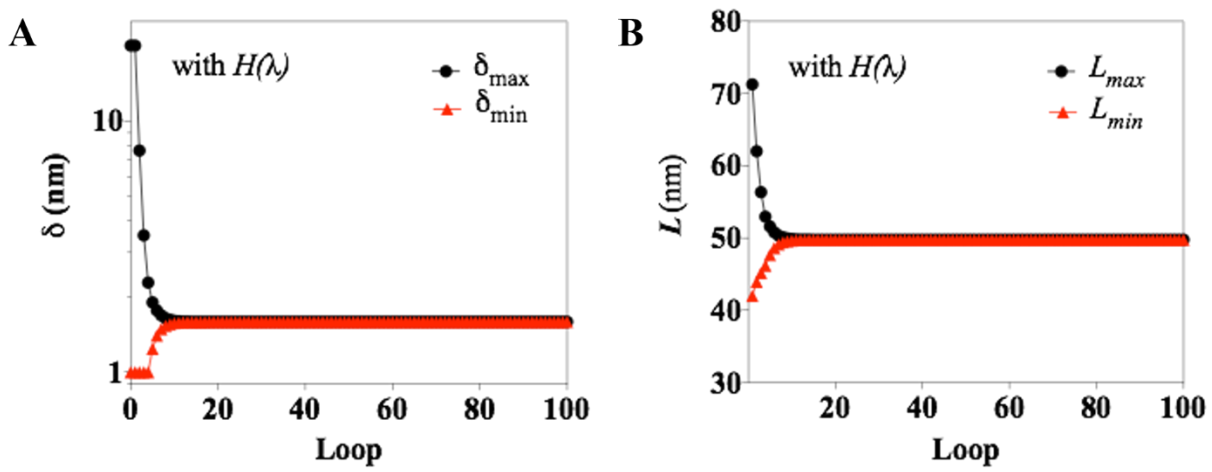

Fig. S6. Determination of the geometrical variables *L* and δ through a reverse Monte Carlo method. The minimization was performed between $D_{m,exp}(d)$ and $H(\lambda)D_{m,sim}(d, L, \delta)$ against varied d_{exp}. The parameters (**A**) δ and (**B**) *L* were found to rapidly converge after 10 loops as shown in the figures.

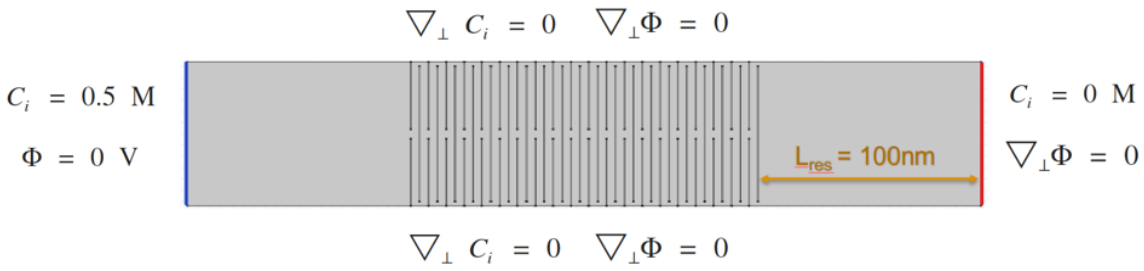

Fig. S7. The continuum simulation model for steady-state diffusion across negatively charged cascading nanoslits. The model consists of 40 layers of impermeable, negatively charged (-2.3 or -56.1 mC/m^2) CCG sheets aligned into an array of cascading nanoslits. The cascading nanoslits were sandwiched between two reservoirs 100 nm in length. The concentration difference was set as 0.5 M, same as in the experiments. The potential at the left end was grounded to zero.

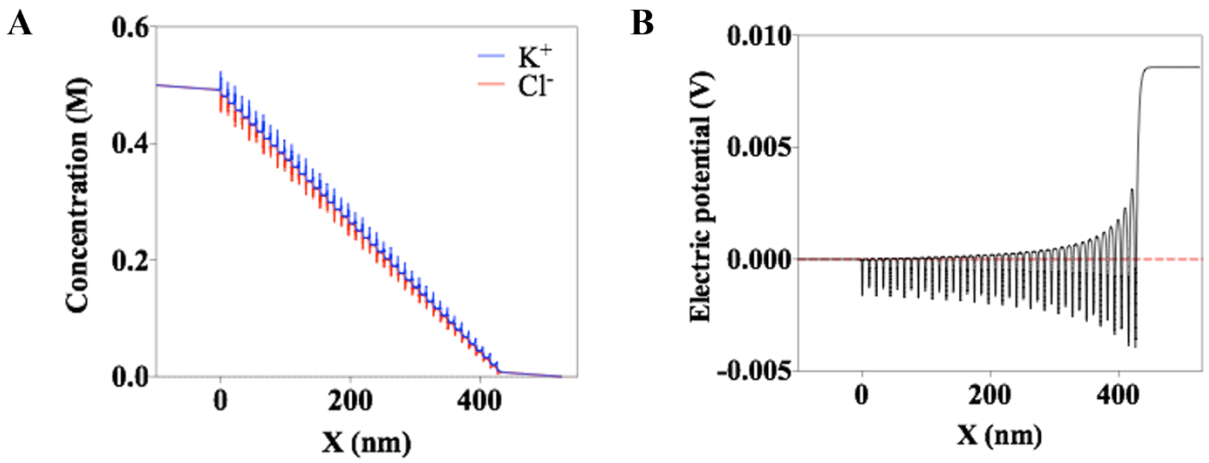

Fig. S8. Concentration and electric potential distribution profiles of the steady-state KCl diffusion across negatively charged cascading nanoslits. (**A**) There is a significant concentration drop across the membrane due to the strongly impeded ion diffusion across the cascading nanoslits. The diffusion of the cations and anions has a similar concentration gradient profile with the abrupt concentration polarization on the surface of CCG sheet, namely Electric Double Layers (EDLs). The negatively charged CCG sheet absorbs counter-ions (K^+) and repels the co-ions (Cl^-). From left to right, the mean concentration in nanoslits gradually decreases with increasing EDL thickness. (**B**) The EDLs also modify the electric potential within the nanoslits, with the lowest value found at the negatively charged CCG surfaces. The formation of EDLs also influences the steady-state diffusion of KCl through the cascading nanoslits. It causes an excess of cations in the channel, which leads to their accumulation in the permeate reservoir, increasing the electric potential (Donnan potential). Such an increase in the Donnan potential, in turn accelerates the diffusion of Cl^- and impedes that of K^+. Thus when the steady-state is reached, the influences of the EDLs and the Donnan potential counteract with each other and minimize their combined effect on diffusion caused by the surface charge of CCG-channel walls.

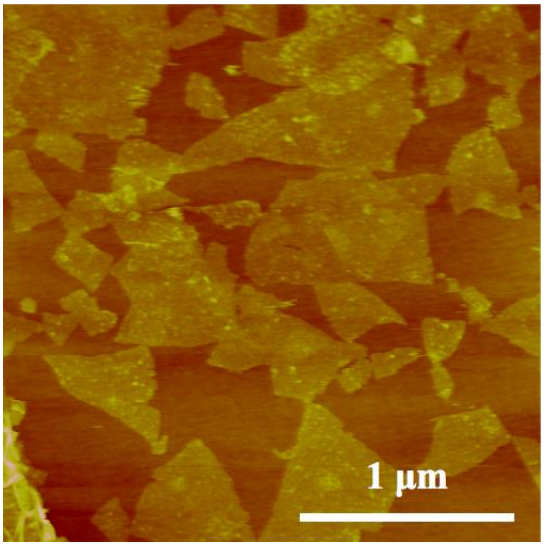

Fig. S9. An AFM image of CCG on mica substrates. The image shows the irregular shape and a broad distribution of the lateral size of the chemically converted graphene nanosheets.

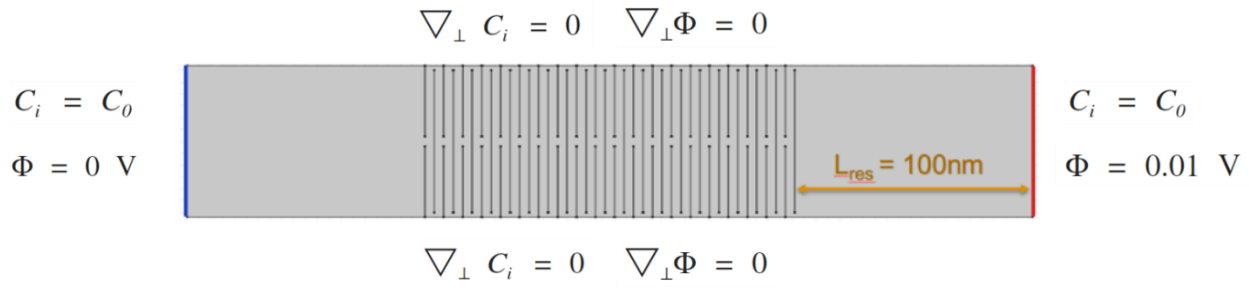

Fig. S10. Continuum simulations of the electrokinetic ion flow across negatively charged cascading nanoslits. The model consisted of 40 layers of impermeable CCG sheets aligned into cascading nanoslits. The cascading nanoslits were sandwiched in between two reservoirs, 100 nm in length. Concentrations in the cascading nanoslits were initially set the same as that in the reservoirs. The potential at the left end was grounded to zero.

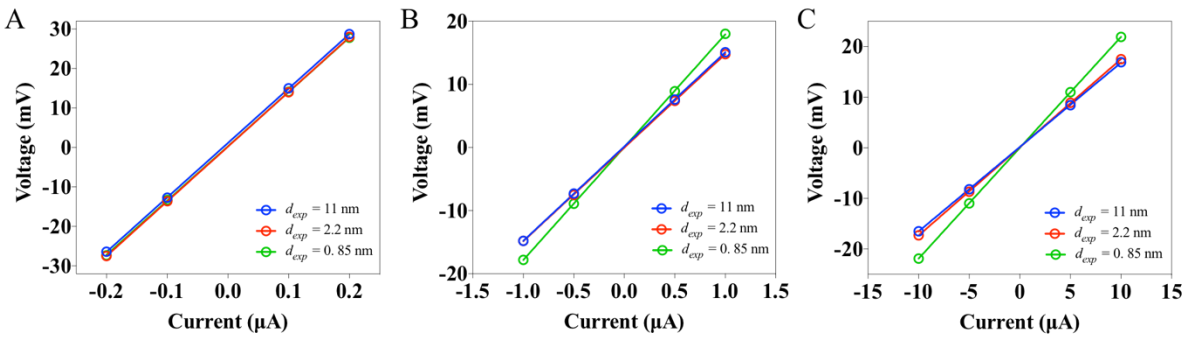

Fig. S11. Representative *I-V* curves of the electrokinetic ion transport measurements. The electrolyte used is (**A**) 1 mM, (**B**) 10 mM and (**C**) 100 mM KCl aqueous solutions.

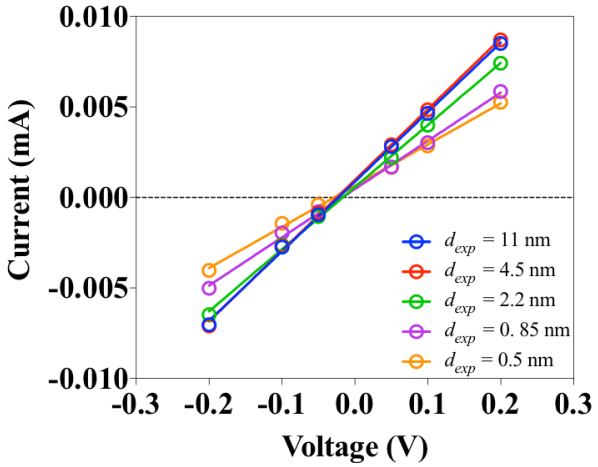

Fig. S12. Typical *I-V* curves for the establishment of membrane selectivity. The *I-V* curves were recorded under a tenfold concentration gradient of K^+ created by putting 10 mM and 100 mM KCl solutions on each side of the membranes. The reverse potential, the potential required to offset diffusion current, for the layered graphene-based membranes are of the order 20~30 mV, indicating that the membranes are cation selective. This cation selectivity is resulted from the negative surface charge status of chemically converted graphene materials when immersed in water.

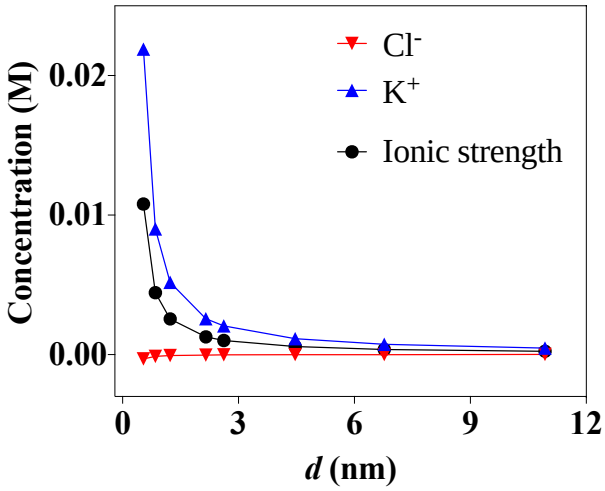

Fig. S13. The increase in channel concentration as a result of channel surface charge. As *d* is reduced below 3 nm, an imbalanced distribution of potassium cations and chloride anions can be observed. As a result, the overall ionic strength in the nanochannel increases, which partially contributes to the enhancement of electrokinetic ion transport observed particularly in highly confined nanospace. The simulation was done in the condition of 1 mM KCl aqueous solution.

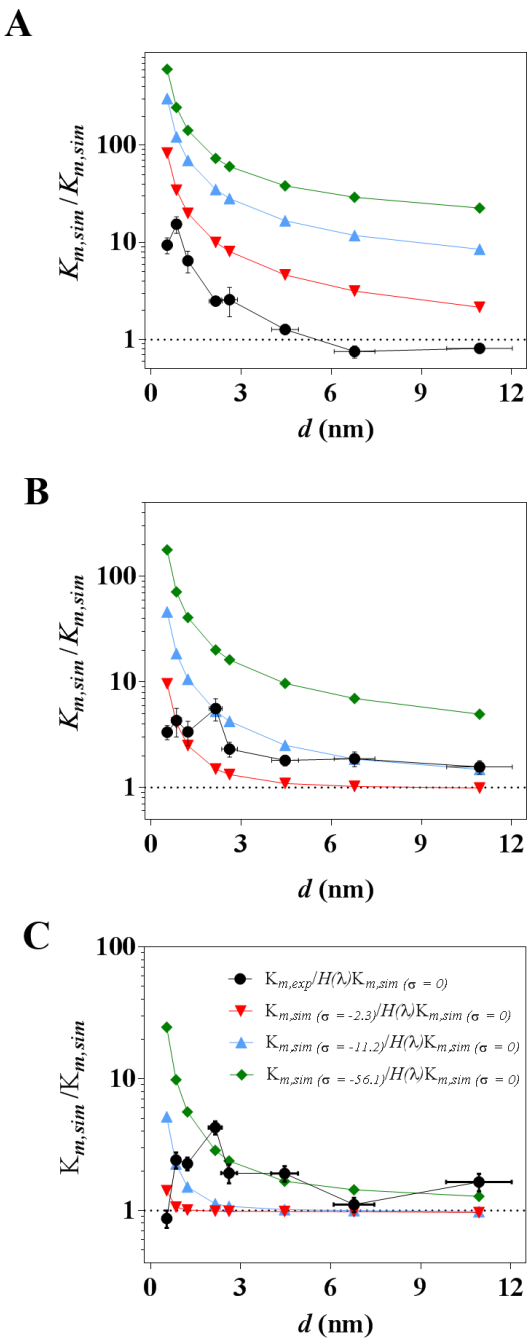

Fig. S14. Scaling behaviors of the electrokinetic ion transport as a function of channel size across the range of sub–10 nm and of varied ionic concentrations. Simulated scaling behaviors of the ion conductivity at sub-10 nm length scales obtained in varied surface charges σ = -2.3 mC/m^2 (red triangles), σ = -11.2 mC/m^2 (blue triangles) and -56.1 mC/m^2 (green diamonds) and varied concentrations, namely (**A**) 1 mM, (**B**) 10 mM and (**C**) 100 mM KCl.

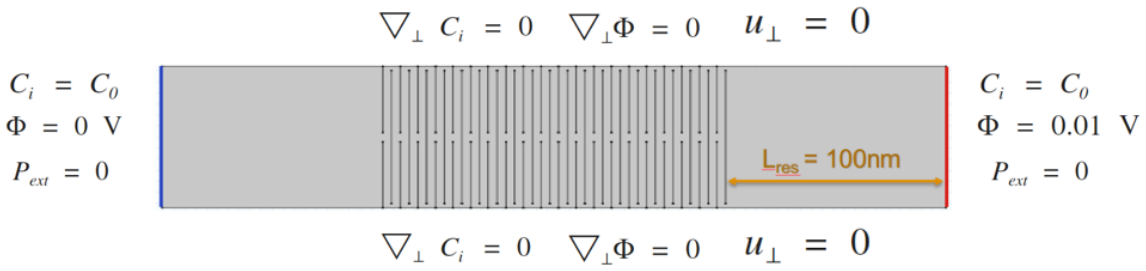

Fig. S15. The continuum simulation model for electroosmotic current across the negatively charged cascading nanoslits. The model consisted of 40 layers of impermeable CCG sheets aligned into cascading nanoslits. The cascading nanoslits were sandwiched in between two reservoirs of 100 nm in length. Concentrations in the cascading nanoslits were set the same as that in the reservoirs. The potential at the left end was grounded to zero. No external pressure was added to the system, and at the top and bottom boundaries there was no tangent shear force for fluidics.

Table S1. Geometries of the cascading nanoslits model

Geometrical variables	***L***	***δ***
without $H(\lambda)$	55 nm	2 nm
with $H(\lambda)$	50 nm	1.6 nm

Table S2. Effect of surface charge status on ion diffusion coefficient across the cascading nanoslits

d (nm)	$D_{KCl,bulk}/D_{m,sim}$		
	Neutral	σ = -2.3 mC m^{-2}	σ = -56 mC m^{-2}
10.934	13.10	13.55	15.07
6.776	24.87	25.42	28.50
4.466	47.26	48.24	55.83